Article

An Evaluation Method of Gas-Bearing Properties Based on Gaussian Bimodal Function Pore Structure Characterization: A Case Study of Tight Sandstone in the East China Sea Basin

Jin Dong [1,2], Zhilong Huang [1,3,*], Jinlong Chen [1,3], Tianjun Li [1,3], Tong Qu [1,3] and Yizhuo Yang [1,3]

1 College of Geosciences, China University of Petroleum, Beijing 102249, China; yyzyangyizhuo0324@163.com (Y.Y.)
2 Research Institute of Petroleum Exploration and Development, China National Petroleum Corporation, Beijing 100083, China
3 State Key Laboratory of Petroleum Resource and Prospecting, China University of Petroleum, Beijing 102249, China
* Correspondence: huangzhilong1962@163.com

Abstract: The Xihu Sag in the East China Sea Basin is located at the edge of the eastern Chinese continent and has great exploration potential. In recent years, the development of low-permeability and tight sandstone gas has become an important area of exploration and development in the Huagang Formation (E3h) of the Xihu Sag. The tight sandstone reservoir in the Xihu Sag is characterized by serious heterogeneity, high water saturation, low resistivity, and a complex gas–water relationship. Because of these characteristics of tight sandstone reservoirs, it is difficult to perform an evaluation of them. In this work, a bimodal Gaussian density function was constructed using the data of high-pressure mercury intrusion (HPMI) and nuclear magnetic resonance (NMR); this approach was used to analyze the pore structure parameters. The reservoirs were divided into four types using the fitting parameter η, and the rock electric parameters that correspond to different pore structures were quite different. When combined with the log response equation of η with acoustic interval transit time (AC), density (DEN), and natural gamma (GR) logging curves, an evaluation method of gas-bearing properties that was based on the characteristics of the pore structure was established. Compared with the water saturation test of the sealing core, it was found that the water saturation calculated by the classification of the pore structure was more accurate than that obtained by the conventional method, and the error was less than 8.35%, which proves that this method is feasible and effective. The findings of this study can help provide a better understanding of the distribution characteristics of gas and water in tight sandstone and provide help for tight gas exploration and development.

Keywords: East China Sea Basin; tight sandstone reservoir; pore structure; bimodal Gaussian density function; evaluation method of gas-bearing properties

1. Introduction

Natural gas is an important part of the transition from traditional fossil fuels to clean energy and is key to achieving China's "carbon peaking and carbon neutrality goals" [1–3]. In recent years, with the rapid development of exploration theory and extraction technology, the proven reserves and production of natural gas have been further increased [4,5]. The developed gas reservoirs are mainly medium- to high-permeability reservoirs, having the properties of good reservoir quality, high production, and economic efficiency. The undiscovered and undeveloped gas reservoirs are mainly tight sandstone gas reservoirs, having poor reservoir quality, low production, and even requiring specific methods such as fracturing and horizontal wells for production assistance [6,7]. The discovery of medium- to high-permeability gas reservoirs is gradually decreasing, and the newly discovered reserves are mainly low-permeability tight gas reservoirs. To ensure a stable energy supply,

tight sandstone reservoirs have become the focus of exploration and development in the next stage, and enough attention and focused research should be provided to them [8–10].

Previous studies on gas-bearing properties have applied the Archie formula and its derivatives [11–13]. However, the poor physical properties, strong heterogeneity, high bound water saturation, and complex gas–water distribution relationships of tight sandstone gas reservoirs lead to significant changes in rock electrical parameters, and the rock–electric relationship does not conform to the traditional Archie's law. This in turn affects the accuracy of the log interpretation and reservoir evaluation, which results in unsatisfactory oil and gas testing results [11,14]. Rock electrical parameters are influenced by many pore structure factors, such as micro-porosity [15,16], pore space tortuosity [17,18], connectivity, and particle roughness [19–22]. Due to the heterogeneity of tight sandstone reservoirs, reservoir parameters greatly vary in the same area and depth, and it is difficult for a single rock electrical parameter to accurately describe a reservoir's characteristics [21,23]. Previous studies have found that as the pore structure deteriorates, the rock electric parameters change regularly; however, there is still a lack of research on the division of pore structure types and the value of rock electric parameters [23]. Taking the Huagang Formation in the West Lake depression as an example, the porosity distribution ranges from 2.8% to 13.8%, with an average of 8.3%, and the permeability distribution ranges from 0.05×10^{-3} μm^2 to 31.8×10^{-3} μm^2, with a large span of reservoir parameters. When evaluating gas-bearing properties using the Archie formula, corresponding rock electrical parameters should be established based on different pore structure types. This paper presents the characteristics of bimodal Gaussian function fitting parameters from a tight sandstone reservoir in Huagang Formation, which were obtained using a series of reservoir experiments such as high-pressure mercury intrusion (HPMI) and nuclear magnetic resonance (NMR). The method provides a new quantitative characterization method of pore structure and establishes a new method for evaluating gas-bearing properties in the Huagang Formation reservoir based on pore structure classification. Based on the principle of the Archie formula, this method combines the relationship between pore structure type, rock electrical parameters, and the logging identification method of the pore structure to form gas-bearing evaluation formulae for different pore structure reservoirs. The water saturation test of the sealing core in the study revealed that the water saturation that was calculated by the classification of pore structure was more accurate than that obtained by the conventional method; furthermore, the error was less than 8.35%, indicating that the method is accurate and effective and that it provides a more favorable tool for evaluating gas-bearing properties in tight sandstone reservoirs. In conclusion, attention was drawn to the application range of this method. The empirical formulae and rock electrical parameters provided in this paper were calculated from the data of the Huagang Formation in the Xihu Sag. Different regions should have different empirical formulae, which need to be re-fitted and analyzed based on experimental data from each region.

2. Geological Setting

The East China Sea Basin is the largest Mesozoic–Cenozoic petroliferous basin in China's offshore, and it is located at the eastern margin of the Chinese continent. The Xihu Sag is a significant hydrocarbon-producing sag with great exploration potential [24,25], and it is located in the northeast of the East China Sea Basin with an area of 59,000 km^2 [26] (Figure 1). The Xihu Sag is closed by the Hupijiao Uplift, Changjiang Sag, Haijiao Uplift, and Yushan Uplift in the west, by the Taiwan–Sinzi Fold Belt in the east, by the Diaobei Sag in the south, and by the Fujiang Sag in the north [27]. The Xihu Sag has experienced three tectonic evolution stages: a rifting stage from the Paleocene to the end of the Eocene period, a depression stage from the Oligocene to the end of the Miocene period, and a subsidence stage from the Pliocene period to the present [28,29]. From the bottom up, the stratigraphy in the Xihu Sag is Paleocene (E1), lower Eocene Baoshi Formation (E2b), upper Eocene Pinghu Formation (E2p), Oligocene Huagang Formation (E3h), lower Miocene Longjing Formation (N1l), middle Miocene Yuquan Formation (N12y), upper Miocene

Liulang Formation (N13l), Pliocene Santan Formation (N2s), and Quaternary Donghai Formation (Qd) [30] (Figure 1). The target formation E3h is deltaic and lacustrine, with the tight sandstone reservoir being the main component, and it is a significant hydrocarbon reservoir in the Xihu Sag.
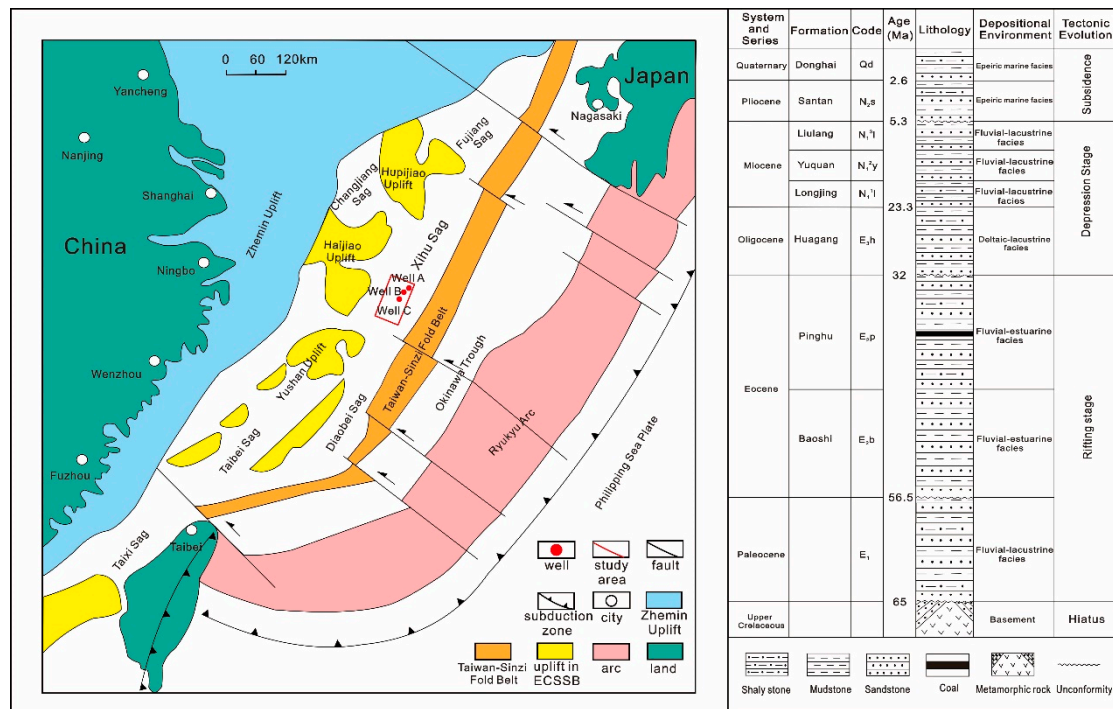
Figure 1. Location map of the study area and the stratigraphy and deposition of the Xihu Sag in the East China Sea (modified after [29]).

3. Experiments and Modeling

According to the data requirements of this research, twenty samples of E3h reservoir drill cores were collected in the depths between 3000 and 4500 m from three wells in the Xihu Sag (Table 1). Various experiments, including routine petrophysical measurements, HPMI, NMR, and bimodal Gaussian density formula fitting, were performed on the samples to characterize the microscopic pore structure of tight sandstone reservoirs in the study areas.

Reservoir physical properties, including porosity and permeability, are the basic parameters for rock properties. The data of the porosity and permeability were measured in cylindrical cores with a diameter of 2.5 cm. According to the American Petroleum Institute standard (API RP-40), the PoroPDP-200 Pulse decay permeameter was used to measure the porosity and permeability.

HPMI is widely used to analyze and evaluate the characterization of pore throat structure. This experiment recorded the amount of mercury intrusion at different pressure equilibrium states to obtain the capillary pressure curve. The pore throat radius can be obtained based on the capillary pressure conversion formula to characterize the pore structure [31,32]. Twenty samples underwent HPMI analysis using an AutoPore III 9505 pore size analyzer. The maximum intrusion pressure was 200.33 MPa, corresponding to a pore throat radius of 3.7 nm.

NMR is a technology used to detect pore structure by measuring the amplitude and relaxation rate of the nuclear magnetic resonance relaxation signal of the hydrogen nuclei in pore fluid based on the principle of interaction between the magnetic properties of the hydrogen nuclei and the applied magnetic field. According to the theory of NMR, the transverse relaxation time of water in a single pore can be converted into the pore radius [33,34]. A longer T_2 relaxation time corresponds to a larger pore size, whereas a small pore size is represented by a shorter T_2 relaxation time; in this way, the pore

size distribution of a reservoir can be characterized by the T_2 spectrum. The specific experimental conditions and parameters included the resonance frequency being set as 12.80 MHz, the magnet strength being set as 0.301 T, a coil diameter of 25 mm, a magnet temperature of 32 °C, a time of echo (TE) of 0.15 ms, and an echo number of 16,000. The SIRT algorithm was adopted in this paper, and the number of inversions was selected to be 200. After measuring the water-saturated NMR, the samples were centrifuged at 3000 r/min for 30 min with the corresponding capillary pressure of about 8.71 psi; the T_2 distributions were also measured [35]. The centrifugal NMR data can be used to distinguish bounded fluid pores and movable fluid pores.

Table 1. Microscopic pore structure parameters from the HPMI and NMR analysis of E3h tight sandstones in the Xihu Sag.

Well	Depth/m	Porosity/%	Permeability/$\times 10^{-3} \mu m^2$	Maximum Mercury Saturation/%	Maximum Radius/μm	Average Radius/μm	Entry Pressure/Mpa	Median Pressure/Mpa	$T_{2cutoff}$/ms	Movable Fluid Saturation/%	Movable-Fluid Porosity/%
A-1	3450.7	8.20	1.95	79.02	9.19	1.80	0.08	0.84	6.69	65.68	5.39
A-1	3830.5	12.60	1.66	99.22	3.68	0.99	0.20	0.96	6.69	58.14	7.33
A-2	3983.6	8.50	0.16	81.61	0.49	0.17	1.50	10.52	11.57	42.46	3.61
A-2	3600.72	10.84	11.88	67.41	13.35	3.12	0.06	4.39	3.41	69.81	7.57
A-2	3600.72	10.72	7.48	57.65	8.91	2.08	0.08	19.38	3.18	70.00	7.50
A-2	3961.62	5.13	0.17	79.20	1.07	0.28	0.69	10.46	2.25	43.13	2.21
A-2	3980.48	8.61	0.96	94.82	2.80	0.70	0.26	1.52	5.54	50.22	4.32
A-2	3980.48	9.41	1.03	80.29	2.80	0.72	0.26	2.51	2.25	62.66	5.90
A-2	4322.24	4.32	0.18	98.16	1.08	0.26	0.68	3.17	3.41	46.83	2.02
A-3	4120.2	6.10	0.08	66.25	0.49	0.13	1.50	39.34	6.69	56.34	3.44
A-4	3508.4	2.80	0.05	55.19	0.49	0.12	1.50	89.67	11.57	50.44	1.41
A-4	3915.1	7.20	0.95	80.01	2.45	0.53	0.30	3.39	6.69	62.84	4.52
B-2	3743.3	13.80	31.80	99.78	10.50	3.98	0.07	0.19	13.89	55.85	7.71
B-2	4000.2	3.50	0.07	87.19	0.37	0.14	2.00	9.28	13.89	15.97	0.56
B-2	4001.2	7.10	0.25	92.20	0.74	0.20	1.00	5.60	13.89	15.97	1.13
B-2	3742.45	12.64	28.86	78.74	13.36	4.16	0.06	1.07	2.58	71.71	9.06
B-2	3742.45	12.84	23.49	88.85	13.36	4.54	0.06	0.27	2.58	71.15	9.14
B-3	4292.7	7.00	0.12	98.61	0.74	0.19	1.00	4.39	13.89	45.25	3.17
C-1	3981.8	7.10	0.12	77.88	0.37	0.11	2.00	11.01	5.57	51.77	3.68
C-1	3989.6	6.90	0.20	83.92	0.49	0.17	1.50	6.20	4.64	57.87	3.99

A rock electric experiment is important for determining rock electric parameters in the Archie formula. The Archie formula has two basic principles: the resistivity of water-saturated reservoir is proportional to the resistivity of formation water, having a coefficient called the formation factor F; and the resistivity of oil- and gas-saturated reservoirs is proportional to the resistivity of formation water, having a coefficient called the resistivity index I. In this experiment, cylindrical rock core samples with a length of 5 cm and a diameter of 2.5 cm were used. After being washed, dried, and weighed, the dry weight of the sample was determined and the air permeability and porosity were measured. Then, the rock sample was placed in the vacuum process chamber, where it was vacuumed for 2 h and saturated with formation water for 24 h. The formation water used had a salinity of 8000 mg/L and a resistivity of 0.655 Ω·m at 26 °C. The rock sample saturated with 100% formation water was weighed to calculate its pore volume. Next, the rock sample was placed in the pressure vessel to calculate the water saturation and resistivity within the rock sample at 0.01 MPa of pressure. This process was repeated at the pressures of 0.02 MPa, 0.03 MPa, 0.04 MPa, 0.05 MPa, 0.09 MPa, 0.20 MPa, 0.70 MPa, and 1.2 MPa. Based on these data, the relationship between the resistivity, water saturation, porosity, and formation factors were determined, and the parameters of the Archie formula could be determined.

The bimodal Gaussian function considers the NMR curve as two Gaussian density functions with six variables that are related to T_2. By fitting the experimental data, empirical formulae relating the parameters to porosity and permeability can be obtained, and the pore

structure can be predicted and characterized by using the logging porosity and permeability. The Gaussian bimodal function curve Equation (1) is as follows:

$$P(log\ T_2; W_1, log\mu_1, log\sigma_1; W_2, log\mu_2, log\sigma_2)$$

$$p = W_1 * \frac{1}{\sqrt{2\prod}*\log\sigma_1} * e^{-\frac{(\log T_2 - \log\mu_1)^2}{2*(\log\sigma_1)^2}} + W_2 * \frac{1}{\sqrt{2\prod}*\log\sigma_2} \tag{1}$$

$$* e^{-\frac{(\log T_2 - \log\mu_2)^2}{2*(\log\sigma_2)^2}}$$

where T_2 is the transverse relaxation time in *ms*; P is signal proportion as a dimensionless value; and W_1 and W_2 are the weighting coefficients of a single Gaussian function. W_2 represents the fraction of the large pore volume, which mainly determines the flow capacity and permeability. W_1 represents the fraction of the small pore volume, in which irreducible water is mainly retained in the centrifugal nuclear magnetic experiment; it shows the small contribution to the fluid flow. $logu_1$ and $logu_2$ are the logarithmic radius averages of the small pore volume and large pore volume, respectively; generally, a larger value indicates a larger pore volume, which contains a larger flow channel and higher conductivity. $log\sigma_1$ and $log\sigma_2$ are the logarithmic standard deviations of the smaller pore volume and larger pore volume, respectively, and they indicate the heterogeneity of the pore size; a larger values indicate poor pore sorting and a higher tortuosity of the pore network, resulting in a lower permeability under the same condition of pore medium radius and pore volume.

4. Results and Discussion

4.1. Reservoir Property

The reservoir property refers to the porosity and permeability, which are important parameters for evaluating reservoir storage and flow performance. The porosity of 20 core samples from the Huagang Formation in the Xihu Sag ranged from 2.8% to 13.8%, mainly being concentrated in the range from 5% to 10% with an average porosity of 8.3% (Table 1). The permeability ranged from 0.05×10^{-3} μm^2 to 31.8×10^{-3} μm^2, being mainly concentrated in the range from 0.1×10^{-3} μm^2 to 1×10^{-3} μm^2 with an average permeability of 5.57×10^{-3} μm^2 (Figure 2). According to the evaluation method for oil and gas reservoirs in China (SY/T6285—2011), the Huagang Formation in the Xihu Sag is mainly composed of tight sandstone reservoirs. Previous studies have also indicated that the reservoirs in the Huagang Formation mostly meet the definition of tight sandstone reservoirs, with porosity < 10% and permeability < 1×10^{-3} μm^2. In summary, the reservoirs in the Huagang Formation are mainly tight sandstone reservoirs with some local low- and medium-porosity/permeability reservoirs.
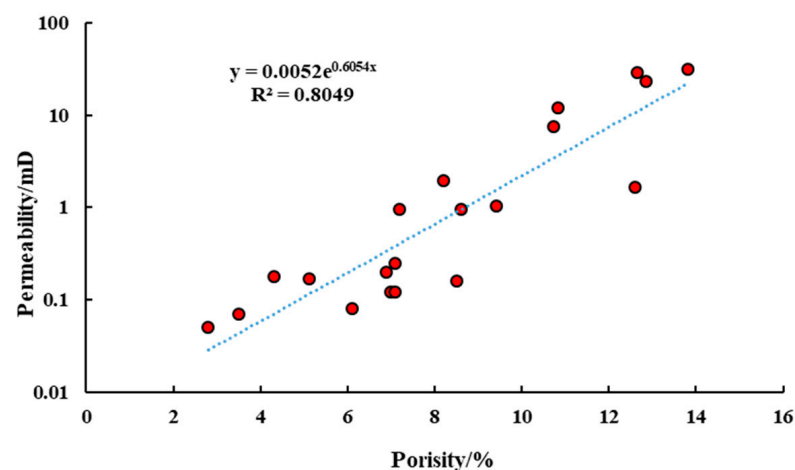
Figure 2. Relationship between porosity and permeability of the E3h tight sandstone reservoirs in Xihu Sag.

4.2. Pore Throat Structure Characteristics

4.2.1. Pore Throat Network Characteristics from HPMI

Figure 3 shows the mercury injection curves of the 20 core samples from the Huagang Formation in Xihu Sag. An analysis of the HPMI curves and data found that the mercury injection curves of the samples have similar trends. In the early stage of mercury injection (mercury saturation of less than 30%), the mercury injection curves reached entry pressure and then remained almost horizontal (platform period) for a long time. The longer the platform period, the more concentrated the pore throat radius distribution of the core samples, indicating better sorting. The lower the location of the platform period, the larger the pore throat radius and the lower the entry pressure of the samples. After the mercury saturation reached 40–50%, the curve slope increased and the mercury injection volume growth slowed down, gradually reaching the maximum mercury saturation. The curves of the samples vary in shape, with significant differences occurring in the experimental parameters, including maximum mercury saturation, maximum throat radius, entry pressure, average throat radius, and median pressure, which indicates a strong heterogeneity of the Huagang Formation reservoirs in the Xihu Sag (Table 1). The maximum mercury saturations of the samples varied from 55.19% to 99.78% with an average of 82.3%, with 80% of the samples being concentrated between 80 and 100%. The entry pressure ranged from 0.06 MPa to 2 MPa with an average of 0.74 MPa. The average throat radius spanned a wide range from 0.11 µm to 4.54 µm and was mainly concentrated between 0.1 µm and 0.5 µm. The median pressure ranged from 0.19 MPa to 89.67 MPa and was mainly concentrated between 0.1 MPa and 5 MPa. Figure 4 shows that the permeability is negatively correlated with entry pressure (R^2 = 0.92) and median pressure (R^2 = 0.53) and positively correlated with average throat radius (R^2 = 0.96). The larger the entry pressure and median pressure, the smaller the samples' average throat radius and permeability. The distribution of the pore throat radius for the samples is wide, and 60% of the samples are concentrated between 0.1 µm and 1 µm, while the remaining 40% of the samples are concentrated between 1 µm and 10 µm. The pore throat radius distribution is concentrated in larger pore throats for high-porosity and high-permeability samples. In the samples with a permeability of greater than 1×10^{-3} µm², the pore throat radii are concentrated at 2 µm. On the other hand, in samples with a permeability of less than 1×10^{-3} µm², the pore throat radii are concentrated between 0.25 µm and 0.5 µm. These findings indicate that pore throat distribution is an important factor affecting reservoir permeability.
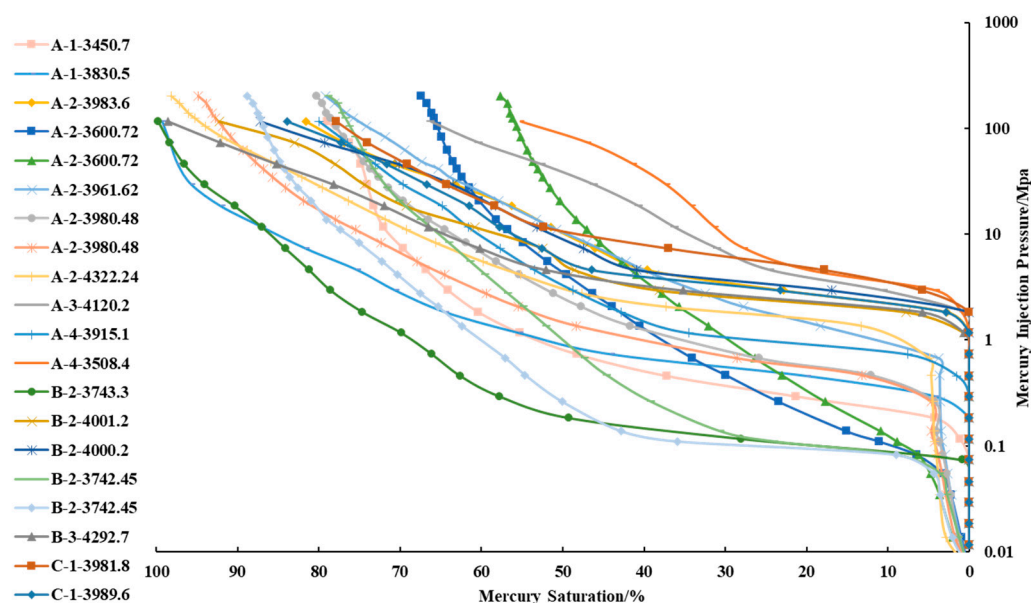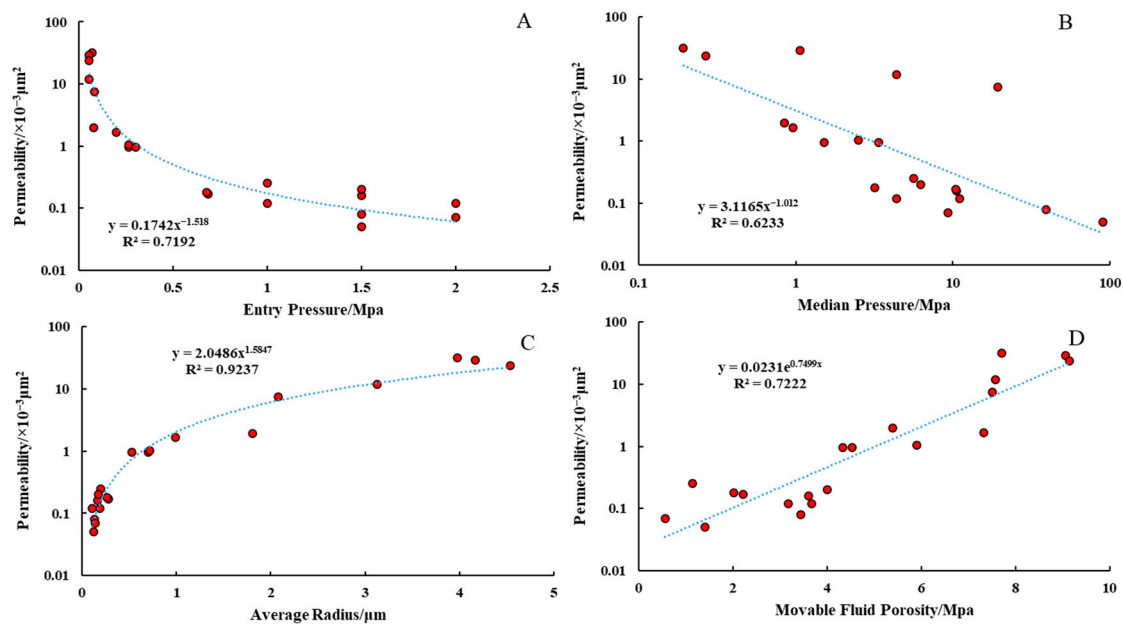

Figure 3. The mercury intrusion curves of the twenty samples as obtained from the HPMI analysis.

Figure 4. Plot showing the relationships between (**A**) entry pressure and permeability; (**B**) median pressure and permeability; (**C**) average radius and permeability; (**D**) movable fluid porosity and permeability.

4.2.2. Pore Size Distributions from NMR

Table 1 summarizes the nuclear magnetic parameters, including the nuclear magnetic pore volume, T_2 cutoff value, movable porosity, bound water saturation, and other parameters. The T_2 cutoff value ranged from 3.22 ms and 13.89 ms with an average of 7.04 ms. The movable fluid porosity showed a wide range from 0.56% to 9.14% with an average of 4.68%. The bound water saturation ranged from 28.29% and 84.03% with an average of 46.3%. The sample's pore size distribution ranged widely and mainly followed the bimodal distribution (Figure 5). The left peak was concentrated between 0.69 ms and 13.92 ms, while the right peak was concentrated between 14.31 ms and 163.99 ms. The interval between the two peaks suggests that the pore distribution was discontinuous and that the sorting of the pores was poor. Comparing the T_2 spectra of water-saturated and centrifugation samples, the results showed that the right peak corresponded to large pores with a long T_2 relaxation time and good connectivity, which mainly resided in movable water. During centrifugation, the signal intensity of the right peak is very low, indicating that most of the water has been removed. On the contrary, the left peak corresponds to shorter T_2 relaxation times, which were attributed to small pores and poor connectivity. During centrifugation, the signal intensity of the left peak remains strong, indicating a large amount of irreducible water that resides in it. By comparing the sample data, it can be found that the T_2 spectra of high permeability samples were dominated by the right peak, which showed small T_2 cutoff values and large movable fluid porosity. On the other hand, the T_2 spectra of samples with poor permeability were dominated by the left peak, which showed large T_2 cutoff values and small movable fluid porosity. These observations indicate that well-connected large pores corresponding to the right peak have significantly contributed to the reservoir permeability, while poorly connected micropores corresponding to the left peak have a smaller contribution to the reservoir permeability but have a great impact on reservoir porosity, which is consistent with the HPMI data.
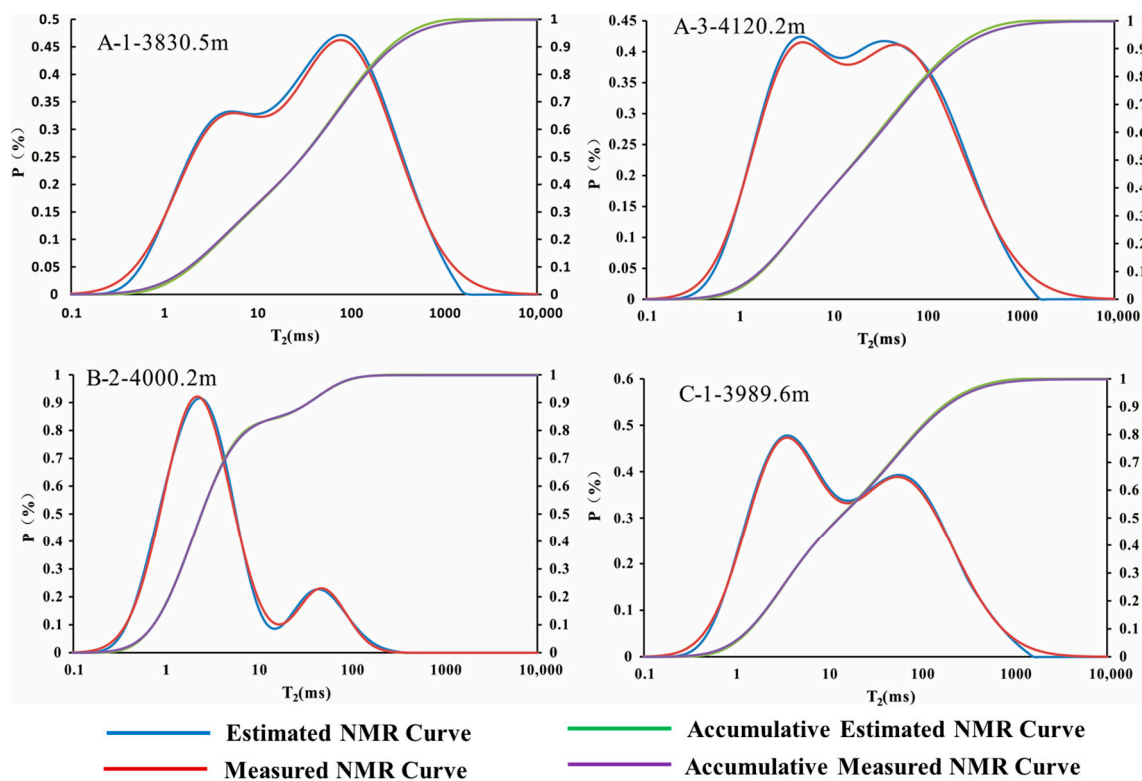
Figure 5. Gaussian fitting results of some samples.

### 4.3. Gaussian Bimodal Function Fitting

Using the fitting function of Origin software, we combed the T_2 spectrum and Gaussian bimodal function curve equation and obtained various fitting parameters (Table 2). Comparing the measured curve with the fitted curve (Figure 5) showed that the fitting function had a high fitting rate with the measured curve. Furthermore, the R^2 values were generally greater than 0.99, which reflects that the fitted curves were extremely close to the measured curve and can reflect the characteristics and properties of the measured curve. Then, the T_2 spectrum can be converted into a pore radius distribution by using a fixed conversion coefficient and the HPMI data. Figure S1 shows that the converted cumulative T_2 spectrum and cumulative mercury injection curve fit well and that their distribution curves have similar trends, indicating a good fitting effect.

Table 2. The parameters of the bimodal Gaussian density function.

| Well	Depth/m	Porosity/%	Permeability /$\times 10^{-3}$ μm²	$log u_1$/ms	$log \sigma_1$	W_1/%	$log u_2$/ms	$log \sigma_2$	W_2/%	$log d_1$ /μm	$log d_2$ /μm	R^2	Type
A-1	3450.70	8.20	1.95	0.61	0.49	0.38	1.93	0.54	0.62	0.11	2.37	1.00	II
A-1	3830.50	12.60	1.66	0.59	0.48	0.35	1.92	0.57	0.65	0.05	1.13	1.00	II
A-2	3983.60	8.50	0.16	0.49	0.39	0.70	1.61	0.42	0.30	0.04	0.58	1.00	III
A-2	3600.72	10.84	11.88	0.24	0.58	0.43	1.80	0.53	0.57	0.09	3.20	1.00	I
A-2	3600.72	10.72	7.48	0.19	0.55	0.42	1.74	0.56	0.58	0.09	3.19	1.00	II
A-2	3961.62	5.13	0.17	−0.03	0.51	0.71	1.22	0.61	0.29	0.07	1.27	1.00	IV
A-2	3980.48	8.61	0.96	−0.16	0.48	0.37	1.31	0.68	0.63	0.03	0.82	0.99	II
A-2	3980.48	9.41	1.03	−0.15	0.49	0.38	1.34	0.68	0.62	0.03	0.90	1.00	II
A-2	4322.24	4.32	0.18	−0.03	0.50	0.42	1.16	0.92	0.58	0.03	0.47	1.00	IV
A-3	4120.20	6.10	0.08	0.51	0.42	0.35	1.72	0.64	0.65	0.02	0.38	1.00	IV
A-4	3508.40	2.80	0.05	0.52	0.45	0.37	1.86	0.58	0.63	0.03	0.57	1.00	IV
A-4	3915.10	7.20	0.95	0.59	0.49	0.36	1.92	0.56	0.64	0.04	0.92	1.00	II
B-2	3743.30	13.80	31.80	0.71	0.62	0.54	1.88	0.44	0.46	0.18	2.62	1.00	I
B-2	4000.20	3.50	0.07	0.34	0.37	0.85	1.68	0.26	0.15	0.04	0.92	1.00	IV
B-2	4001.20	7.10	0.25	0.34	0.37	0.85	1.68	0.26	0.15	0.04	0.94	1.00	III
B-2	3742.45	12.64	28.86	0.18	0.65	0.46	1.73	0.46	0.54	0.09	3.03	0.99	I
B-2	3742.45	12.84	23.49	0.25	0.64	0.48	1.70	0.43	0.52	0.10	2.84	1.00	I
B-3	4292.70	7.00	0.12	0.41	0.41	0.47	1.72	0.50	0.53	0.03	0.70	1.00	IV
C-1	3981.80	7.10	0.12	0.48	0.39	0.49	1.72	0.56	0.51	0.02	0.42	1.00	IV
C-1	3989.60	6.90	0.20	0.49	0.40	0.44	1.76	0.58	0.56	0.02	0.38	1.00	III

Table 2 shows the fitting parameters with a varied distribution. The $logd_1$ ranged from 0.02 μm to 0.38 μm with an average of 0.10 μm. The $log\sigma_1$ varied from 0.37 to 0.65 with an average of 0.48. The W_1 ranged from 0.35% to 0.85% with an average of 0.49%. The $logd_2$ showed a wide range from 0.38 μm to 4.58 μm with an average of 1.8μm. The $log\sigma_2$ ranged from 0.26 to 0.92 with an average of 0.54. The W_2 varied from 0.15% to 0.65% with an average of 0.51%. The fitting parameters quantitatively characterized the pore structure and were closely related to the reservoir's permeability, which had a good correlation with the parameters of the HPMI and NMR data. The $logd_2$ reflects the average radius of well-connected larger pores. The larger the $logd_2$ value, the better the permeability of the samples. The $logd_2$ score had a significant positive correlation with movable fluid porosity ($R^2 = 0.61$) and average throat radius ($R^2 = 0.81$) and a negative correlation with entry pressure ($R^2 = 0.81$) and bound water saturation ($R^2 = 0.44$) (Figure 6). The $logd_1$ score showed a similar trend, which had a positive correlation with movable fluid porosity ($R^2 = 0.41$) and average radius ($R^2 = 0.69$) and a negative correlation with entry pressure ($R^2 = 0.60$) (Figure S2). On the one hand, when the $logd_1$ increased, it indicated that the average radius of poorly connected small pores increased, which also increased the sample's permeability. On the other hand, there was a close relationship between $logd_1$ and $logd_2$ ($R^2 = 0.71$). Although the differences between $logd_1$ and $logd_2$ were not fixed in different samples, the range was small, being concentrated between 0.36 μm and 4.19 μm. Samples with a large $logd_2$ generally had a large $logd_1$, so the $logd_1$ exhibited a similar regularity to $logd_2$.
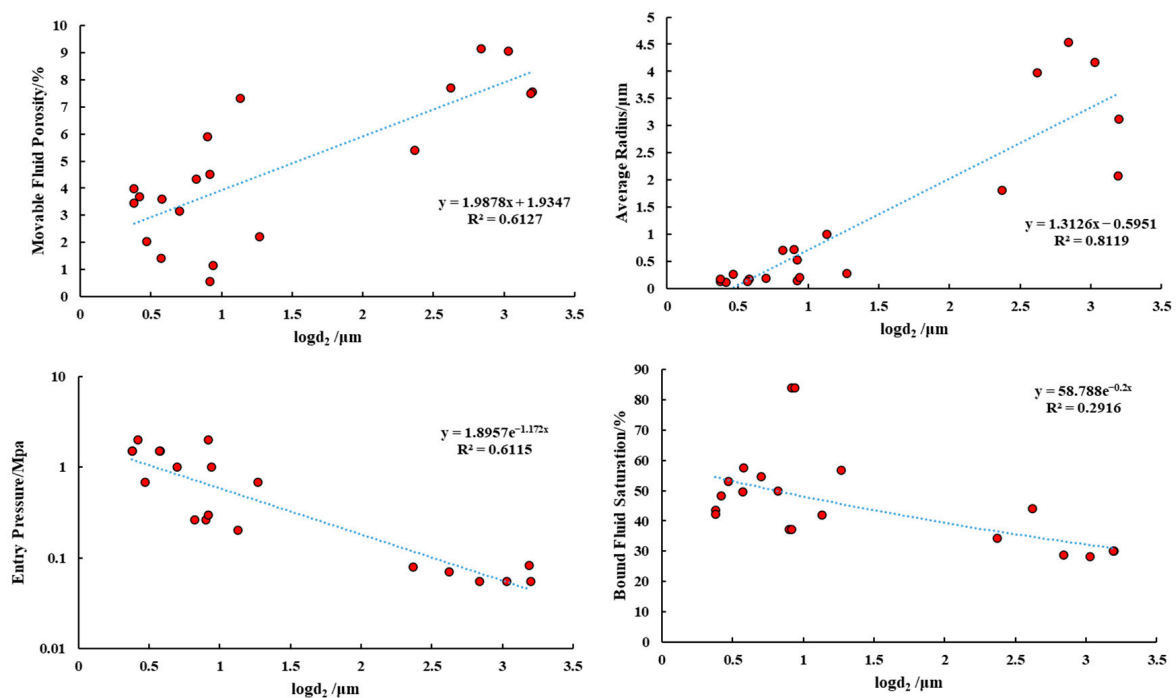
Figure 6. Correlations between $logd_2$ and movable fluid saturation, average throat radius, displacement pressure, and bound water saturation.

This study also found that the correlation between W_2 and other experimental parameters was not strong (Figure S3). This is because the sum of W_1 and W_2 is 100% and because they only reflect the individual proportions of large pores and small pores. Some samples may have a high proportion of large pores but have low porosity, resulting in poor permeability. On the other hand, some samples may have a small proportion of large pores but have high total porosity, indicating that the porosity of the large pores is still high and that their permeability is great. Therefore, when using W_1 and W_2 to evaluate the pore structure, it is best to multiply it by porosity, converting it to $\varphi^* W_2$ (porosity of the large pore), which is more practical. The porosity of the large pores reflected the

movable fluid and had strong correlations with the parameters of the HPMI and NMR data, which had positive correlations with movable fluid porosity ($R^2 = 0.87$) and average radius ($R^2 = 0.64$) and negative correlations with displacement pressure ($R^2 = 0.64$) and bound water saturation ($R^2 = 0.64$) (Figure 7). These indicated that as the porosity of the large pore increased, the reservoir quality improved. The correlations between $\varphi^* W_1$ (porosity of the small pores) and various parameters were weaker than those of $\varphi^* W_2$.
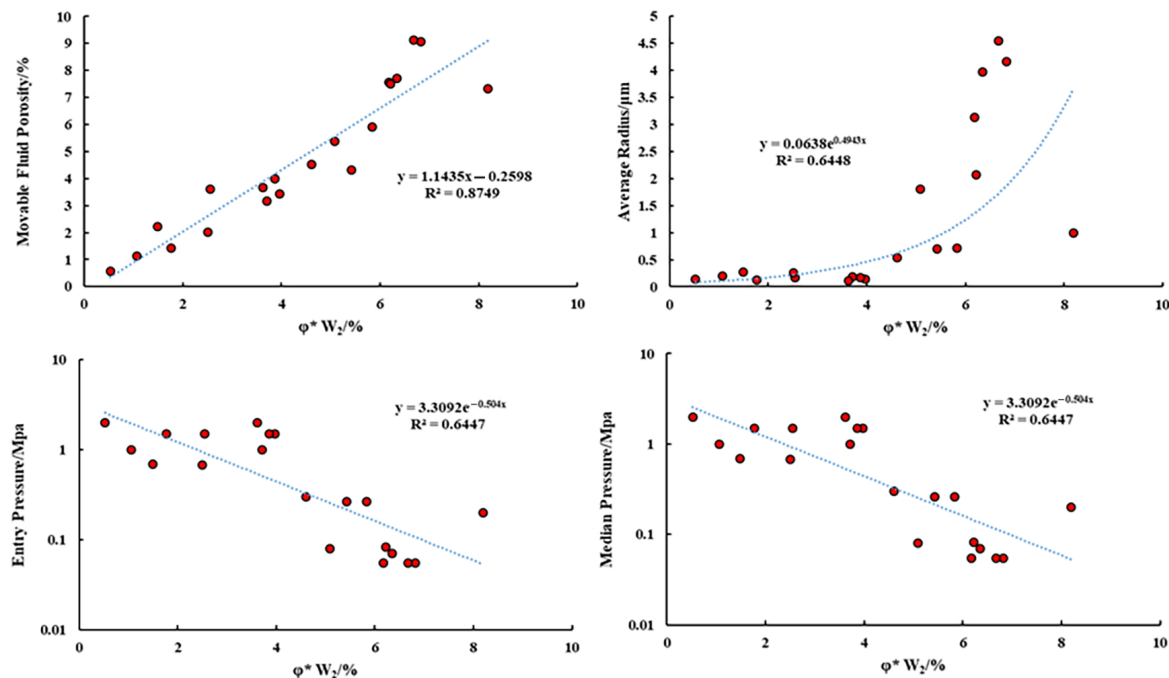
Figure 7. Correlations between $\varphi^* W_2$ and movable fluid saturation, average throat radius, entry pressure, and median pressure.

*4.4. Classification of Reservoirs Based on Pore Structure*

By analyzing the experimental data, four types of pore structures were classified in the E3h reservoirs. According to previous studies, $\varphi^* W_2$ indicated the amount of movable fluid and $logd_2$ reflected the average radius of well-connected large pores. Both $\varphi^* W_2$ and $logd_2$ were part of the reservoir quality evaluation indicators and had a good correlation with reservoir permeability. Only one parameter may lead to deviations in reservoir evaluation. To comprehensively evaluate the pore structure, the concept of a comprehensive pore structure index η value (Equation (2)) was introduced as follows:

$$\eta = \varphi^* W_2 {}^* logd_2 \tag{2}$$

The η value was an evaluation parameter that combined the proportion of movable fluid and the radius of the large pores. The η value shows a significant positive correlation with permeability ($R^2 = 0.9$), movable fluid saturation ($R^2 = 0.82$), and average throat radius ($R^2 = 0.9$) and a negative correlation with entry pressure ($R^2 = 0.87$) (Figure 8). These indicated that the larger the η value, the better the reservoir pore structure, the stronger the permeability, and the higher the reservoir quality. Reservoir quality and pore structure can be effectively evaluated by the η value, and four types of pore structures were classified: type I, type II, type III, and type IV (Figure 9) (Table 3).

There were three type I samples, which accounted for 15% of the total number of samples; the porosity was generally greater than 12% and the permeability was greater than $10 \times 10^{-3} \ \mu m^2$. The mercury injection curve of type I is in the lower-left corner of Figure 3, with entry pressures of lower than 0.08 MPa and an average entry pressure of 0.06 MPa. The curves showed a three-stage pattern, with a long stable platform period

in the early stage of mercury injection. After the mercury saturation reached 40–45%, the amount of mercury intrusion rapidly increased and mercury intrusion curves showed a larger slope. The average maximum mercury saturation reached 89.12%. Overall, the pore throat radius was large, with an average throat radius of 4.23 μm. The pore throats had good connectivity, and the pore structure was relatively simple with good sorting. At the same time, the NMR curve showed that the curve is dominated by the right peak, with an average $logd_2$ of 2.83 μm. The type I samples had strong permeability with an average movable fluid porosity of 8.64%, indicating that the reservoir was excellent.
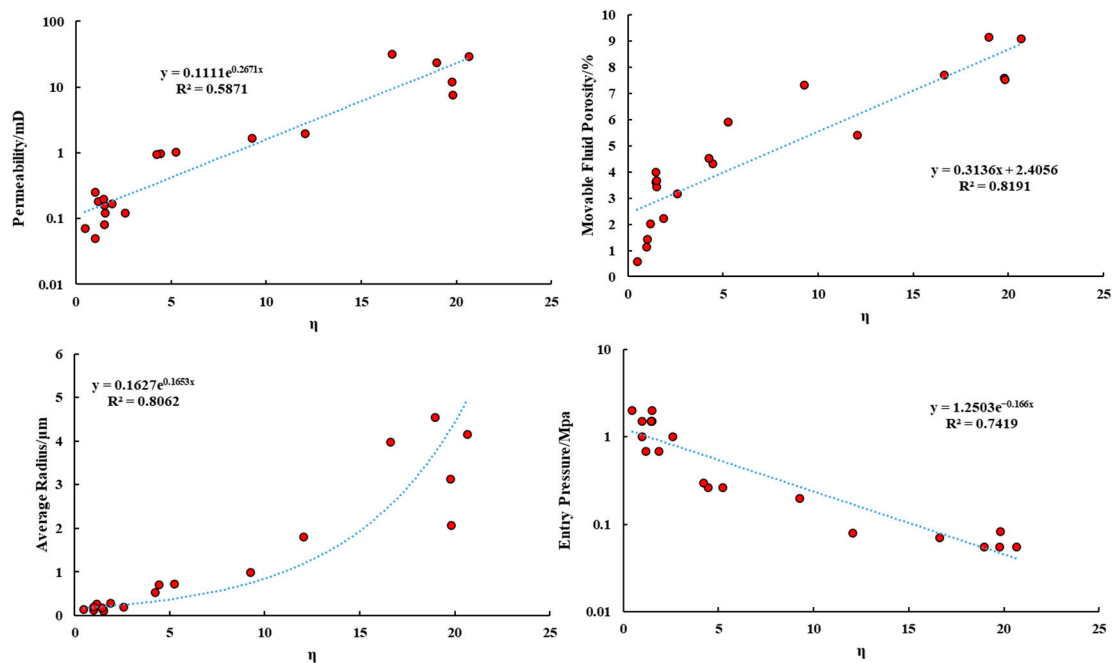
Figure 8. Correlations between η and permeability, porosity of movable fluid, average throat radius, and entry pressure.
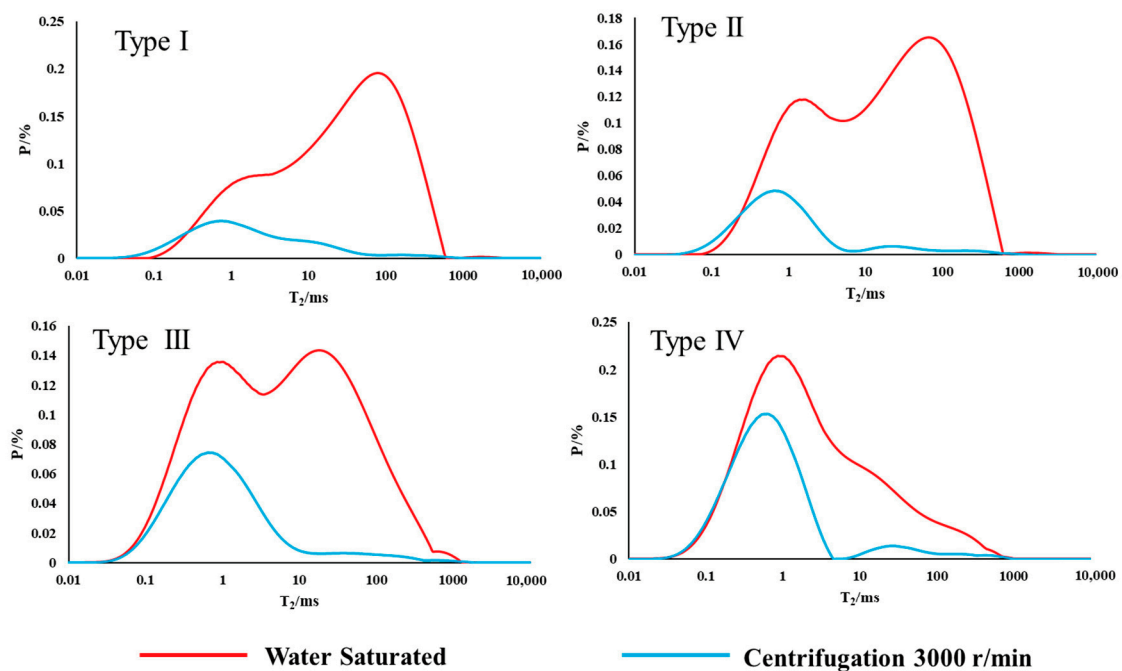
Figure 9. Characteristics of T_2 spectra with different pore structure types.

Table 3. Classification of pore structures in the Huagang Formation.

Classification Parameters	Classification of Pore Structure			
	I	**II**	**III**	**IV**
η	>18	18~8	8~2	<2
Porosity/%	>15	15~10	10~5	<5
Permeability/$\times 10^{-3}$ μm^2	>10	10~1	1~0.2	<0.2
Entry Pressure/Mpa	<0.1	0.1~0.2	0.2~1	>1
Average Radius/μm	>2	2~0.7	0.7~0.2	<0.2
Movable Fluid Porosity/%	>11	8~11	4~8	<4
Reservoir Evaluation	Excellent	Good	Fair	Poor

There were four type II samples, which accounted for 20% of the total number of samples, with the porosity generally ranging from 8% to 10% and the permeability ranging from 1×10^{-3} μm^2 to 10×10^{-3} μm^2. The mercury injection curve of type II is located slightly higher than type I, with the entry pressures ranging from 0.08 MPa to 0.2 MPa and an average entry pressure of 0.1 MPa. Similar to type I, the early stage of mercury injection also had a long stable platform period. After the mercury saturation reached 50%, the slope of the mercury intrusion curves gradually increased and the average maximum mercury saturation reached 75.83%. The pore throat radius was relatively large, with an average throat radius of 2 μm. The pore structure was moderate with medium sorting. The NMR curve of type II is bimodal, with an average $logd_2$ of 2.47 μm. The samples of type II had relatively strong permeability, with an average movable fluid porosity of up to 6.95%, indicating a good reservoir.

There were five type III samples, which accounted for 25% of the total number of samples, with the porosity generally ranging from 5% to 10% and the permeability ranging from 0.2×10^{-3} μm^2 to 1×10^{-3} μm^2. The mercury injection curve of type III is in the upper right region of Figure 3, with entry pressures ranging from 0.2 MPa to 1 MPa and an average entry pressure of 0.67 MPa. The NMR curve of type III is also bimodal, but the left peak dominates the curve in some samples, with an average $logd_2$ of 1.85 μm. The type III samples had poor permeability, with an average movable fluid porosity of up to 3.97%, indicating that the reservoir was fair.

There were seven type IV samples, which accounted for 40% of the total number of samples, with the porosity generally being less than 7% and the permeability being less than 0.2×10^{-3} μm^2. The mercury injection curve of type IV was higher than other types, with entry pressures being generally larger than 0.2 MPa and an average entry pressure of 1.36 MPa. The platform period of the curve is relatively short and fuzzy, and the average maximum mercury saturation can reach 80.51%. The pore throat radius was small, with poor sorting and pore structure, and the average throat radius was 0.17 μm. The NMR curve is dominated by the left peak, with an average $logd_2$ of 0.66 μm. The samples of type IV had terrible permeability, with an average movable fluid porosity of up to 2.51%, indicating poor reservoir quality.

Based on the statistical analysis of the experimental data of core samples and the testing data from MDT, it was found that the average permeabilities of type I and type II were 18.89 mD and 3.04 mD, respectively, with average gas saturations being 44.6% and 35.5%, respectively; these results indicate that these reservoirs were predominantly gas-bearing. The average permeabilities of type III and type IV were 0.36 mD and 0.14 mD, respectively, with average gas saturations being 29% and 19.7%, respectively, indicating that these reservoirs were dominated by water-bearing pores. Type I and type II reservoirs were considered effective reservoirs, with type I being the higher-quality reservoir. However, most reservoirs of type III and type IV were considered non-effective reservoirs.

4.5. Logging Response of Reservoir Classification

Before evaluating the gas-bearing properties of reservoirs, the reservoirs need to be classified by the pore structure parameter η and the logging data. For the reservoirs of the

Huagang Formation in the study area, the classification method of the pore structure can be divided into two types: NMR logging and no NMR logging. In some areas where NMR logging is available, the reservoirs can be directly classified by using the NMR logging curve for the Gaussian function fitting to obtain the η value.

Most areas of the Xihu Sag lacked the NMR logging data required, and it was necessary to use conventional logging data to fit the η value and classify the pore structure of the reservoirs in the target formation. The η value was closely related to porosity and clay content, mainly because the porosity parameter was applied in the construction of the η value parameter. Porosity directly affects reservoir quality, and the increase in clay content can reduce reservoir permeability and porosity (Figure S4). By utilizing the relationship among these three parameters, a logging fitting formula for the η value can be constructed. AC and DEN logging curves are commonly used to calculate porosity. AC logging measures the propagation velocity of compressional waves in the formation, which can reflect the lithology, porosity, and fluid properties of the formation. DEN logging typically uses cesium (CS) as a gamma ray source to measure the absorption intensity of gamma rays by the formation to determine the density of the formation lithology. GR logging is a method of measuring the natural gamma ray intensity of the formation along the wellbore. In the Huagang Formation reservoirs, there are no other radioactive minerals except for clay minerals, and the radioactivity in the rock is mainly determined by the clay content; thus, the GR logging curve can be used to determine the clay content in the reservoir. Therefore, by combining the AC, DEN, and GR logging curves, the η value can be fitted (Figure S5).

By combining the η values and the corresponding logging curve values at different depths, a multivariate linear regression analysis was conducted using SPSS software (Figure 10). As a result, the logging fitting formula for the η value (Equation (3)) can be obtained:

$$\eta = -192.381 + 1.158AC + 60.942DEN - 146.569\triangle GR \quad R^2 = 0.856 \tag{3}$$

where $\triangle GR$ is the normalized value of the relative gamma ray curves, and its calculation formula is as follows (Equation (4)):

$$\triangle GR = \frac{GR - GR_{min}}{GR_{max} - GR_{min}} \tag{4}$$

where $\triangle GR$ is the normalized value of GR logging (dimensionless); GR is the natural gamma ray logging value of the target layer (API); GRmax is the maximum GR value of each well in the target layer, (API); and GRmin is the minimum GR value of each well in the target layer (API). By using the fitting formula of the η value, the type of pore structure for the entire well length of the no NMR logging well can be classified, which lays the foundation for gas content evaluation.
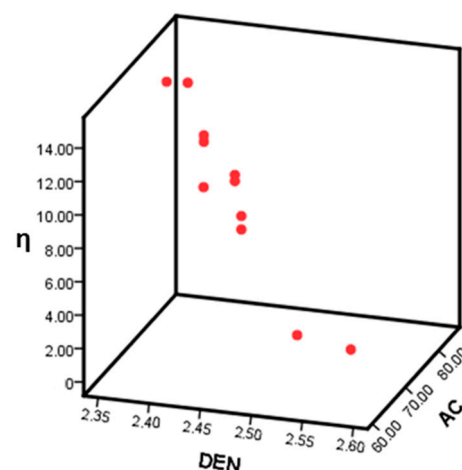

Figure 10. Fitting chart of η with DEN and AC.

4.6. The Influence of Pore Structure on Rock Electrical Parameters

Thirty samples were used for rock electrical experiments at normal temperature and pressure. During the experiments, the formation factor was calculated, which ranged from 27.19 to 119.41 with an average of 61.62. Figure 11 shows the relationship between porosity and the trend line of the samples calculated, where $a = 3.3596$ and $m = 1.1690$. Under the pressure displacement of 1.2 MPa, the water saturation of the samples ranged from 23.75% to 88.53%, indicating significant differences in pore structure among the samples. The differences of b for the samples were small, which ranged from 0.99 to 1.03 with an average of 1.01. Meanwhile, the differences in n were large, varying from 1.4 to 2 with an average of 1.61. By establishing a single relationship between the water saturation and resistivity index for the 30 samples, the values of b and n were calculated as $b = 1.0242$ and $n = 1.4916$. According to the traditional calculation method, the rock electrical parameters of the Huagang Formation reservoirs were as follows: $a = 3.3596$, $b = 1.0242$, $m = 1.1690$, and $n = 1.4916$. The value of a exceeds the empirical range of Archie's parameter, and there is a significant variation in the n for individual samples. These findings indicate that there was a large error in uniformly calculating the parameters of the Archie formula without classifying the pore structure differentiation. Therefore, for complex pore structures in tight sandstone reservoirs, different rock electrical parameters should be used based on different types of pore structures.
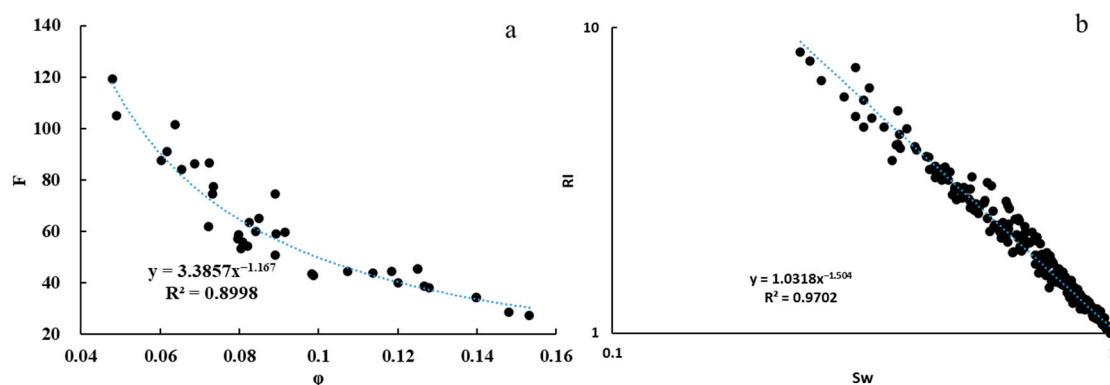
Figure 11. (**a**) Correlations between formation factor and porosity; (**b**) Correlations between formation resistivity factor and water saturation.

Based on the classification of pore structure, the rock electrical parameters of samples were recalculated (Figure 12), and significant differences were found among samples with different pore structures. As the reservoir quality deteriorated, the values of a and n gradually increased, while the values of b and m tending to decrease. Among the rock electrical parameters, the variation in b was the smallest, while the values of a and m varied greatly among different types of pore structures. For type I: $a = 0.6352$, $m = 2.006$, $b = 1.092$, $n = 1.498$; for type II: $a = 1.2534$, $m = 1.614$, $b = 1.038$, $n = 1.465$; for type III: $a = 1.5359$, $m = 1.469$, $b = 1.022$, $n = 1.466$; and for type IV: $a = 1.8513$, $m = 1.37$, $b = 1.011$, $n = 1.64$ (Table 4). Previous studies showed that under the same conditions of temperature, pressure, and mineralization of formation water, the pore structure is an important influencing factor for a and m. The m value reflected the tortuosity of pores in samples, and different shapes and networks resulted in different m values. Because the changes in the a and m parameters had opposite effects on F, they were negatively correlated. The n value reflects the wettability of samples, in which the values of n in oil-wet rocks were higher than those of hydrophilic rocks and the values of n in highly water-saturated sandstone were greater than those in low water-saturated sandstone.
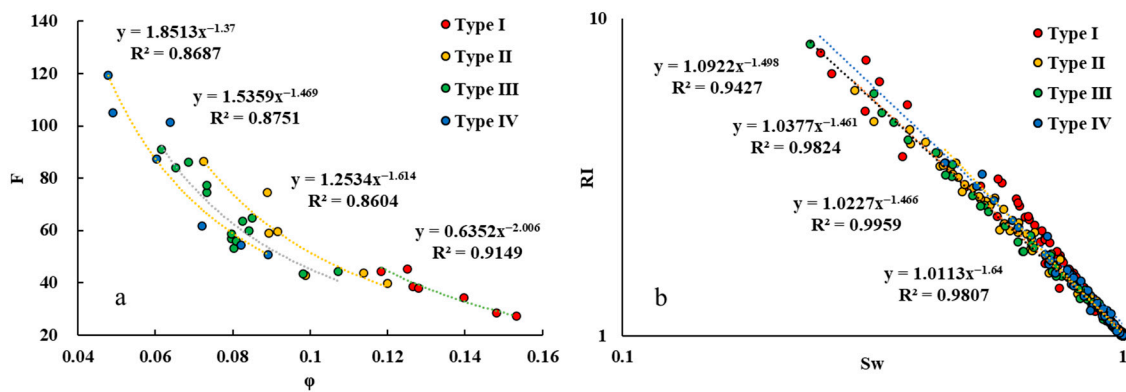
Figure 12. (**a**) Correlations between formation factor and porosity with different pore structure types. (**b**) Correlations between formation resistivity factor and water saturation with different pore structure types.

Table 4. Characteristics of rock electric parameters with different pore structure types.

Type	Rock Electrical Parameters			
	a	*b*	*m*	*n*
I	0.635	1.092	2.006	1.498
II	1.253	1.038	1.614	1.461
III	1.536	1.022	1.469	1.466
IV	1.851	1.011	1.37	1.64

4.7. Method for Gas-Bearing Properties Based on Pore Structure

In this study, significant differences were found in the rock electrical parameters in different types of pore structures. If the rock electrical parameters of different pore structure types were mixed in the calculations, there would be significant deviations, which would lead to an overestimation of formation gas-bearing properties and difficulty in accurately identifying gas layers. Therefore, this study first used conventional logging curves to fit the η value based on core sample experimental data and identified the type of pore structure. Different rock electrical parameters were selected for the calculation to ensure the accuracy of gas-bearing properties. The procedure was as follows:

(1) Collect core samples and experimental data, test the physical properties and NMR of the core samples, and then establish the measured nuclear magnetic curve based on the experimental data.
(2) Fit and calculate the parameters (W_1, $log\mu_1$, $log\sigma_1$, W_2, $log\mu_2$, $log\sigma_2$) of the NMR curve and calculate the η value to classify the sample pore structure.
(3) Rock electric experiments were used for different types of pore structures to determine the variations in rock electrical parameters.
(4) For areas with NMR logging data, the values of η can be obtained by Gaussian function fitting to classify the pore structure of the target reservoir.
(5) For areas without NMR logging data, the values of η can be obtained by establishing a logging fitting formula and then classifying the pore structure of the target reservoir.
(6) Based on the classification of pore structure, varying rock electrical parameters should be selected for different types of reservoirs; then the water saturation of the target reservoir should be calculated to determine the gas-bearing properties.

The complex pore structure and strong heterogeneity of tight sandstone makes it difficult to effectively characterize the pore structure of reservoirs using conventional methods; the Archie formula is also unable to accurately calculate water saturation. The reservoir pore structure can be decomposed into six parameters in Gaussian bimodal function fitting, which can quantitatively evaluate the reservoir pore structure. Then, the value of η can be calculated and used to classify the pore structure, which reflects the

percolation flow capacity of the reservoir, solving the puzzle of tight sandstone reservoir characterization and evaluation. Based on the NMR data and well logging data such as AC, DEN, and GR, the empirical formulae for predicting the reservoir quality can be established, which solves the puzzle of reservoir evaluation in some areas that lack NMR logging data.

It should be noted that this method applies to conventional, low-permeability, and tight sandstone reservoirs and does not consider carbonate, volcanic, and metamorphic rock reservoirs; it cannot be simply applied to these types of reservoirs and requires a re-evaluation of the principles. The bimodal Gaussian function was used in the function fitting because the pore size distribution in tight sandstone was predominantly bimodal. Although there may be rare samples with unimodal pore size distribution, we can refer to the other samples of similar depth to determine whether the unimodal peak represents large or small pores. In areas with NMR logging data, the Gaussian functions can be fitted by the NMR logging data, and η can be calculated to evaluate the pore structure. In areas without NMR logging data, it is necessary to establish a correlation between conventional well logging curves and η values based on NMR experimental data. The empirical formulae for fitting η using conventional well logging data and rock electrical parameters for different types of pore structures in the above research were calculated based on data from the Xihu Sag in the East China Sea. Different regions should have different empirical formulae, which need to be re-fitted and analyzed based on experimental data from each region.

4.8. Example Verification

To validate the accuracy of this method, a comparison was performed between the sealing core data, conventional Archie formula calculations, and calculations based on pore structure classification. A sealing core refers to a drilling core obtained without contamination from drilling fluids using specialized sealing core tools. A sealing core ensures that the core can provide accurate information on original porosity, oil and gas saturation, and other data. By comparing the sealing core data from three depths in Well A-2 (4317.67 m to 4325.07 m), Well A-4 (3506.56 m to 3514.61 m), and (3910.38 m to 3918.57 m), it was found that the calculation error of water saturation when using the conventional Archie formula reached 16.56% (Figure 13) with a significant overestimation of water saturation in some reservoirs. In contrast, the error of the new method proposed in this paper was reduced to 8.35% (Figure 13), which had a lower error and higher accuracy than the conventional method.
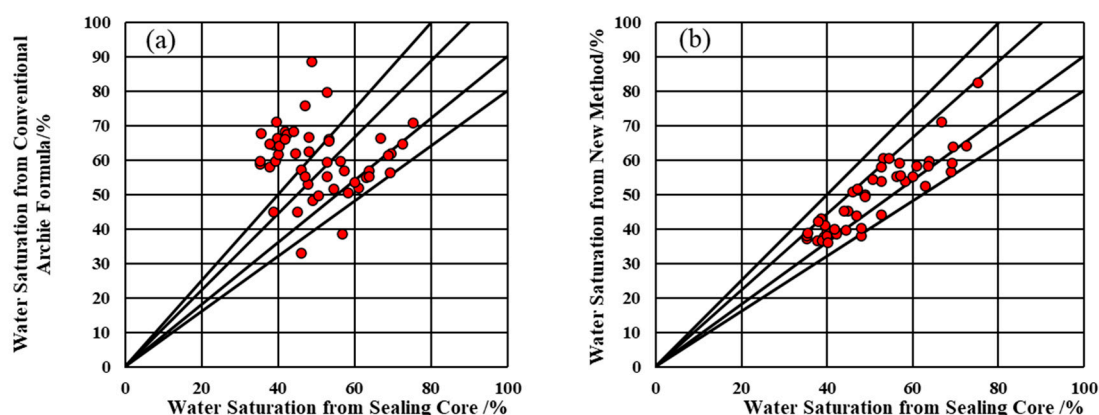
Figure 13. (**a**) Comparison of water saturation between that predicted by the Conventional Archie formula and that measured in the sealing core; (**b**) comparison of water saturation between that predicted by the new method and that measured in sealing core.

5. Conclusions

The reservoirs in the Huagang Formation of the Xihu Sag are mainly composed of tight sandstone reservoirs, with porosities ranging from 2.8% to 13.8% and an average porosity of 8.3%; the permeability ranged from 0.05×10^{-3} μm^2 to 31.8×10^{-3} μm^2 with an

average of 5.57×10^{-3} μm^2. Based on HPMI and NMR experiments, a Gaussian bimodal function fitting curve was constructed, and the fit parameters (φ, W_2, $logd_2$) were selected to establish a composite parameter η to classify the reservoir into four types of pore structures. The fit parameters and η values for different types of reservoirs show significant differences.

With respect to the classification of pore structure and the experimental data of rock electricity, it was found that the rock electric parameters corresponding to different pore structures are quite different. The *a* and *m* values changed greatly, *with a* increasing from 0.64 for type I to 1.85 for type IV and *m* decreasing from 2 for type I to 1.37 for type IV. However, the variation of *b* and *n* are small.

This study established the calculation formula of η with AC, DEN, and GR and identified the type of pore structure in the whole wells. Afterwards, the gas saturation of the reservoirs was calculated according to the different pore structures with various rock electric parameters, and the evaluation of gas-bearing properties of the Huagang Formation was completed based on the characteristics of the pore structure. According to the identification and calculation, the Huagang Formation is mainly composed of type II and type III reservoirs and a small amount of type I reservoirs locally. Compared with the water saturation test of the sealing core, the validity of the method was verified. It was found that the water saturation calculated by the classification of pore structure is more accurate than that of the conventional method, and the error is less than 8.35%.

References

1. Chen, B.; Shen, J.; Hao, J.; Du, W. Characteristics of quartz sandstones and its reservoir significance of Xujiahe Formation in Yuanba area, northeastern Sichuan Basin. *Acta Sedimentol. Sin.* **2012**, *30*, 92–100.
2. Jia, C.; Sepehrnoori, K.; Huang, Z.; Yao, J. Modeling and analysis of carbonate matrix acidizing using a new two-scale continuum model. *SPE J.* **2021**, *26*, 2570–2599. [CrossRef]
3. Jiang, L.; Zhao, W.; Bo, D.; Hong, F.; Gong, Y.; Hao, J. Tight sandstone gas accumulation mechanisms and sweet spot prediction, Triassic Xujiahe Formation, Sichuan Basin, China. *Pet. Sci.* **2023**. [CrossRef]
4. Zheng, H.; Liu, Z.; Xu, S.; Liu, Z.; Liu, J.; Huang, Z.; Huang, Y.; Shi, Z.; Wu, Q.; Fan, L.; et al. Progress and key research directions of tight gas exploration and development in Xujiahe Formation, Sinopec exploration areas, Sichuan Basin. *Oil Gas Geol.* **2021**, *42*, 765–783.
5. Feng, L.; Jiang, Y.; Guo, G.; Yang, C.; Zhu, X.; Zeng, Q.; Cai, G.; Wang, Z. Impacts of mineralogy and pore throat structure on the movable fluid of tight sandstone gas reservoirs in coal measure strata: A case study of the Shanxi formation along the southeastern margin of the Ordos Basin. *J. Pet. Sci. Eng.* **2023**, *220*, 111257.
6. Li, P.; Zheng, M.; Bi, H.; Wu, S.; Wang, X. Pore throat structure and fractal characteristics of tight oil sandstone: A case study in the Ordos Basin, China. *J. Pet. Sci. Eng.* **2017**, *149*, 665–674. [CrossRef]
7. Cui, H.; Zhu, S.; Wang, J.; Gao, Y.; Wan, C.; Tong, H. Physical Properties, Pore-Throat Structure, Fractal Characteristics and Their Effects on the Gas-Bearing Capacity of Tight Sandstone: A Case Study from the Northern Tianhuan Depression, Ordos Basin, China. *Nat. Resour. Res.* **2022**, *31*, 1559–1584. [CrossRef]

8. Clarkson, C.; Freeman, M.; He, L.; Agamalian, M.; Melnichenko, Y.; Mastalerz, M.; Bustin, R.; Radlinski, A.; Blach, T. Characterization of tight gas reservoir pore structure using USANS/SANS and gas adsorption analysis. *Fuel* **2012**, *95*, 371–385. [CrossRef]

9. Zou, C.; Zhang, G.; Yang, Z.; Tao, S.; Hou, L.; Zhu, R.; Yuan, X.; Ran, Q.; Li, D.; Wang, Z. Concepts, characteristics, potential and technology of unconventional hydrocarbons: On unconventional petroleum geology. *Pet. Explor. Dev.* **2013**, *40*, 413–428. [CrossRef]

10. Zou, C.; Yang, Z.; Tao, S.; Yuan, X.; Zhu, R.; Hou, L.; Wu, S.; Sun, L.; Zhang, G.; Bai, B. Continuous hydrocarbon accumulation over a large area as a distinguishing characteristic of unconventional petroleum: The Ordos Basin, North-Central China. *Earth Sci. Rev.* **2013**, *126*, 358–369. [CrossRef]

11. Archie, G. The Electrical Resistivity Log as an Aid in Determining Some Reservoir Characteristics. *Trans. AIME* **1942**, *146*, 54–62. [CrossRef]

12. Syed, A.; Syed, H.; Asma, B.; Quaid, K.; Khalid, L. Petrophysical evaluation using the geometric factor theory and comparison with Archie model (Article). *J. Nat. Gas Sci. Eng.* **2020**, *82*, 103465.

13. Zhong, Z.; Reza, R.; Lionel, E.; Matthew, E.; Feng, R. Determination of Archie's cementation exponent for shale reservoirs; an experimental approach. *J. Pet. Sci. Eng.* **2021**, *201*, 108527. [CrossRef]

14. Aboozar, S.; Abbas, H.; Mohammad, J.; Bahram, S. Development of a new model for prediction of cementation factor in tight gas sandstones based on electrical rock typing. *J. Nat. Gas Sci. Eng.* **2021**, *94*, 104128.

15. Gao, Y.H.; Pan, B.Z.; Zhang, L.H.; Fang, C.H. Research and application of the relationship between transverse relaxation time and resistivity index in tight sandstone reservoir. *J. Pet. Sci. Eng.* **2018**, *160*, 597–604.

16. Zhang, L.; Pan, B.; Shan, G.; Guo, Y. Research progress on influencing factors of saturation index n in Archie formula. *Prog. Geophys.* **2023**, *38*, 1247–1256. [CrossRef]

17. Watfa, M.; Youssef, F. An Improved Technique for Estimating Permeability in Carbonates. *Middle East Oil Show.* **1987**, SPE-15732-MS. [CrossRef]

18. Attia, M. Effects of petrophysical rock properties on tortuosity factor. *J. Pet. Sci. Eng.* **2005**, *48*, 185–198. [CrossRef]

19. Diederix, K. Anomalous relationships between resistivity index and water saturations in the Rotliefend sandstone (The Netherlands). In Proceedings of the SPWLA 23rd Annual Logging Symposium, Corpus Christi, TX, USA, 6 July 1982.

20. Toumelin, E.; Torres-Verdin, C. Influence of oil saturation and wettability on rock resistivity measurements: A uniform pore-scale approach. In Proceedings of the SPWLA 46th Annual Logging Symposium, Corpus Christi, TX, USA, 6 July 1982.

21. Xiao, L.; Zou, C.; Mao, Z.; Shi, Y.; Liu, X.; Jin, Y.; Guo, H.; Hu, X. Estimation of water saturation from nuclear magnetic resonance (NMR) and conventional logs in low permeability sandstone reservoirs(Article). *J. Pet. Sci. Eng.* **2013**, *108*, 40–51. [CrossRef]

22. Zhou, X.; Zhang, C.; Zhang, Z.; Zhang, R.; Zhu, L.; Zhang, C. Saturation evaluation method in tight gas sandstones based on diagenetic facies (Article). *Mar. Pet. Geol.* **2019**, *107*, 310–325. [CrossRef]

23. Zhang, F.; Yan, J.; Li, Z.; Geng, B.; Kou, X.; Gao, Z. Analysis of Rock Electrical Parameters and R_w in Archie Formula for Clastic Rock. *Well Logging Technol.* **2017**, *41*, 127–133.

24. Jiang, S.; Li, S.; Chen, X.; Zhang, H.; Wang, G. Simulation of oil–gas migration and accumulation in the East China Sea continental shelf basin: A case study from the Xihu depression. *Geol. J.* **2016**, *51*, 229–243. [CrossRef]

25. Su, A.; Chen, H.; Chen, X.; He, C.; Liu, H.; Li, Q.; Wang, C. The characteristics of low permeability reservoirs, gas origin, generation, and charge in the central and western Xihu Depression, east China Sea basin. *J. Nat. Gas Sci. Eng.* **2018**, *53*, 94–109. [CrossRef]

26. Zhao, Z.; Dong, C.; Zhang, X.; Lin, C.; Huang, X.; Duan, D.; Lin, J.; Zeng, F.; Li, D. Reservoir controlling factors of the Paleogene Oligocene Huagang formation in the north central part of the Xihu Depression, East China Sea Basin, China. *J. Pet. Sci. Eng.* **2019**, *175*, 159–172.

27. Hao, L.; Wang, Q.; Guo, R.; Tuo, C.; Ma, D.; Mou, W.; Tian, B. Diagenetic fluids evolution of Oligocene Huagang Formation sandstone reservoir in the south of Xihu Sag, the East China Sea Shelf Basin: Constraints from petrology, mineralogy, and isotope geochemistry. *Acta Oceanol. Sin.* **2018**, *37*, 25–34. [CrossRef]

28. Zhang, J.; Yu, Y.; Zhang, T.; Zhang, S.; Tang, X. A discussion on the exploration potential of deep basin gas in Xihu sag, East China Sea. *China Offshore Oil Gas* **2013**, *25*, 24–29.

29. Dong, J.; Huang, Z.; Chen, J.; Li, T.; Zhao, J.; Pan, Y.; Qu, T. Pore Structure and Fractal Characteristics of Tight Sandstone: A Case Study for Huagang Formation in the Xihu Sag, East China Sea Basin, China. *Energies* **2023**, *16*, 2013. [CrossRef]

30. Qian, W.D.; Sun, Q.L.; Stuart, J.; Yin, T.J.; Zhang, C.M.; Xu, G.S.; Hou, G.W.; Zhang, B. Diagenesis and controlling factors of Oligocene Huagang Formation tight sandstone reservoir in the south of Xihu sag, the East China Sea Shelf Basin. *J. Pet. Sci. Eng.* **2022**, *215*, 110579. [CrossRef]

31. Washburn, E.W. Note on a method of determining the distribution of pore sizes in a porous material. *Proc. Natl. Acad. Sci. USA* **1921**, *7*, 115–116. [CrossRef]

32. Nooruddin, H.A.; Hossain, M.E.; Hasan, A.; Okasha, T. Comparison of permeability models using mercury injection capillary pressure data on carbonate rock samples. *J. Pet. Sci. Eng.* **2014**, *121*, 9–22. [CrossRef]

33. Daigle, H.; Thomas, B.; Rowe, H.; Nieto, M. Nuclear magnetic resonance characterization of shallow marine sediments from the Nankai Trough, Integrated Ocean Drilling Program Expedition 333. *J. Geophys. Res. Solid Earth* **2014**, *119*, 2631–2650. [CrossRef]

34. Müller-Huber, E.; Schön, J.; Börner, F. Pore space characterization in carbonate rocks—Approach to combine nuclear magnetic resonance and elastic wave velocity measurements. *J. Appl. Geophys.* **2016**, *127*, 68–81. [CrossRef]
35. Dong, J.; Huang, Z.; Chen, J.; Zhang, W.; Wang, L.; Li, T.; Huang, Q.; Liu, L. A new method to establish NMR T 2 spectrum based on bimodal Gaussian density function: A case study of tight sandstone in East China Sea Basin. *J. Pet. Sci. Eng.* **2018**, *167*, 628–637. [CrossRef]